

Angular-resolved above-threshold-dissociation dynamics by a Fourier-transform grid method with divergent coupling

R. Numico, A. Keller, and O. Atabek

Laboratoire de Photophysique Moléculaire du CNRS, Université Paris-Sud, Campus d'Orsay, Bâtiment 213, 91405 Orsay, France

(Received 13 June 1997)

Angular-resolved fragment kinetic-energy spectra resulting from the photo-dissociation of odd-charged homonuclear ions induced by short, intense laser pulses are calculated using an efficient three-dimensional Fourier-transform method in spherical coordinates. The peculiarity of these ions is their linearly increasing transition dipole moment with the internuclear separation, leading to asymptotically divergent radiative couplings. The method deals with such couplings by splitting the wave function into two regions, an internal and an asymptotic one. The latter is analyzed analytically by a three-dimensional generalization of the Volkov-type solutions of Keller [Phys. Rev. A **52**, 1450 (1995)], while the numerical propagation on the former is performed by combining a contact transformation with the radial and angular grid method of Dateo and Metiu [J. Chem. Phys. **95**, 7392 (1991)]. The procedure basically offers the advantage of a reduced grid extension by avoiding some numerical instabilities and inaccuracies related to the cosine transform of previous algorithms. Unitarity and energy conservation are successfully tested and an application is provided to H_2^+ photodissociation using the Nd:YAG laser (where YAG denotes yttrium aluminum garnet) second harmonic ($\lambda = 532$ nm) at an intensity of 10 TW/cm^2 for which angular-resolved spectra are experimentally available. [S1050-2947(98)00204-2]

PACS number(s): 33.80.Wz, 33.80.Gj

I. INTRODUCTION

The technological possibility to reach large radiation intensities with short pulsed lasers has introduced a completely different situation in the description of the atomic and molecular response to an electromagnetic field [1,2]. Their additional interatomic degrees of freedom and vectorial properties make the study of molecules even more challenging. Very complicated behaviors may be observed even with simple diatomic molecules, such as multiphoton above-threshold dissociation (ATD), which can be evidenced by the observation of peaks in the kinetic-energy spectrum of the atomic photofragments, separated by one quantum of the photon energy [3,4]. Angular distribution of the fragments provide an even more detailed understanding of the laser-molecule interaction, leading, in most cases, to alignment dynamics [5–8].

From the theoretical point of view, nonperturbative approaches such as the construction of the so-called Floquet states [1,9], the time propagation of an initial wave packet [10–13], or a combination of these methods [14] are the most popular ones. Often, complications arising from the strong radiative coupling are much enhanced by the presence of pairs of so-called charge resonant electronic states, as in the case of odd-charged homonuclear ions [15,16], which are considered as good candidates for the study of nonlinear effects [17]. More precisely, their transition dipole moment diverges linearly with their internuclear separation, leading to channels that remain asymptotically coupled and do not represent properly the outcome of the half collision with the particles decoupled from the field. This problem has been addressed recently in the time-independent Floquet scattering approach, considered within the space-translated (or acceleration) frame [18]. Time-dependent approaches not only

provide a proper description of short pulsed lasers, which turn out to be the only way to achieve the high-intensity regime, but also avoid, at least in principle, the previously mentioned asymptotic divergence by the finite duration of the radiative coupling. In practical simulations of kinetic-energy spectra, however, even for short pulse durations, computation times are prohibitive due to very large grids needed to represent the wave-packet motion and spreading. Recently, a propagation method allowing for the description of the entire wave packet using a restricted one-dimensional grid has been proposed [19]. After splitting the wave function into two parts, one corresponding to the internal region and the other to the asymptotic part (following Ref. [20]), the originality of the method consists in an analytic propagation in the asymptotic region even during the laser pulse. The main advantage is that the grid extension is fixed definitively, whatever the duration of the pulse is.

The aim of this paper is to present a Fourier-transform spectral method to solve the time-dependent Schrödinger equation in spherical coordinates by combining a contact transformation with Dateo and Metiu's [21] grid approach for angular degrees of freedom in the inner region. The method of Ref. [19] is generalized for a three-dimensional analytical propagation followed by Fourier analysis in the outer region. The basic ingredients of the theory, with the specific merits of the contact transformation, are presented in the following section together with some numerical convergence, unitarity and energy conservation tests. The method is applied to the photodissociation of H_2^+ by an intense pulse ($I = 10 \text{ TW/cm}^2$) of $\lambda = 532$ nm wavelength delivered by a Nd:YAG laser source (where YAG denotes yttrium aluminum garnet). To the best of our knowledge, this is the first angular-resolved photofragment kinetic-energy spectrum calculation aiming at a detailed interpretation of the experimental observations of Ref. [5].

II. THEORY

Our purpose is to solve the nuclear time-dependent Schrödinger equation on a Born-Oppenheimer level of approximation involving two electronic states labeled g (ground) and u (excited) following, for convenience, the standard symmetry notations of H_2^+ :

$$i\hbar \mathbf{1} \frac{d}{dt} \begin{pmatrix} \Psi_g \\ \Psi_u \end{pmatrix} = \mathbf{H} \begin{pmatrix} \Psi_g \\ \Psi_u \end{pmatrix}, \quad (1)$$

where the total molecule-plus-field Hamiltonian is

$$\mathbf{H} = \mathbf{1}(T_R + T_\theta + T_\varphi) + \mathbf{W}(R, \theta; t). \quad (2)$$

$\mathbf{1}$ is the identity matrix and R, θ, φ are the spherical coordinates of the internuclear vector \vec{R} in the laboratory frame [22]. Kinetic terms are given by

$$T_R = -\frac{\hbar^2}{2m} \frac{d^2}{dR^2}, \quad (3)$$

$$T_\theta = -\frac{\hbar^2}{2m} \frac{1}{R^2 \sin \theta} \frac{d}{d\theta} \left(\sin \theta \frac{d}{d\theta} \right), \quad (4)$$

and

$$T_\varphi = -\frac{\hbar^2}{2m} \frac{1}{R^2 \sin^2 \theta} \frac{d^2}{d\varphi^2}, \quad (5)$$

where m represents the reduced mass. The radiative coupling written in the length gauge involves the scalar product of the dipole moment $\vec{\mu}$ (parallel to \vec{R} for a $\Sigma \rightarrow \Sigma$ transition, as is the case of H_2^+) and the electric field vector $\vec{\mathcal{E}}$, which is taken along the laboratory z axis

$$\vec{\mu} \cdot \vec{\mathcal{E}} = -\mu(R) \cos \theta \epsilon(t) \cos \omega t. \quad (6)$$

The laser pulse carrier-wave frequency is ω and its envelope $\epsilon(t)$ has a Gaussian shape

$$\epsilon(t) = \epsilon_0 e^{-(t-t_0)^2/\tau^2} \quad (7)$$

of half-width τ . The potential part contains the field-free molecular potentials V as diagonal elements and the matter-field couplings as nondiagonal terms:

$$\mathbf{W} = \begin{pmatrix} V_g(R) & -\mu(R) \cos \theta \epsilon(t) \cos \omega t \\ -\mu(R) \cos \theta \epsilon(t) \cos \omega t & V_u(R) \end{pmatrix}. \quad (8)$$

As is clear from Eq. (8), the motion associated with the azimuthal angle φ remains separated under the action of the φ -independent potential term and M_N , the z projection of the total rotation angular momentum N , is a good quantum number describing the invariance through rotation about the field polarization vector. The potential-energy curves are taken from Bunkin and Tugov's fit [23] and the electronic transition moment is taken from Ref. [24]. The initial state of $\text{H}_2^+(^2\Sigma_g^+)$ with an isotropic ensemble of parahydrogen and orthohydrogen in equilibrium involves two components with

$N=1, M_N=0$ (statistical weight of 1/3) and $N=1, M_N=\pm 1$ (statistical weight of 2/3), each of them having to be propagated separately and further combined using their respective weights [22].

A. Propagator

Fourier-transform methodology [10,25] using, for the angular variables, either spherical harmonics basis-set expansions [26] or grid techniques [21,27] is one of the most popular approaches for solving Eq. (1). In particular, Dateo and Metiu have significantly improved the grid approach with an implementation of a unitary Cayley scheme for T_θ combined with a Feit-Fleck split operator technique using a cosine Fourier transform, resulting in a recursion formula [21]. Apart from avoiding the numerical instabilities associated with the division by $\sin \theta$ [Eq. (4)], the major advantage is the absence of matrix element evaluations and multiplications, the computational task being basically fast Fourier transforms. The actions of potential and kinetic operators on the wave function are evaluated by referring to a combination of coordinate and momentum representations, related through an exponential Fourier transform for R and a cosine transform for θ .

A careful examination of this method leads to the following considerations. In the spherical coordinate representation the polar angle θ is defined within the interval $[0, \pi]$. The even parity and 2π periodicity of the cosine transform imply, for the angular part of the wave function,

$$f(\theta) = f(-\theta) = f(2\pi - \theta), \quad (9)$$

from which results a zero-derivative condition at both ends of the interval:

$$\frac{d}{d\theta} f(\theta) \Big|_{\theta=0, \pi} = 0. \quad (10)$$

In other words, as long as Eq. (10) holds, the symmetry requirements are fulfilled and the cosine Fourier representation can be worked out in an accurate way. The actual angular dependence of the wave function is written in terms of spherical harmonics $Y_{N, M_N}(\theta, \varphi)$ satisfying the following relation with respect to their θ derivatives [28]:

$$\frac{d}{d\theta} Y_{N, M_N}(\theta, \varphi) \Big|_{\theta=\pm n\pi} = (-1)^{nN} (\delta_{M_N-1} e^{-i\varphi} - \delta_{M_N+1} e^{i\varphi}) \times \sqrt{\frac{N(N+1)(2N+1)}{16\pi}}, \quad (11)$$

where $n=0$ or $=1$. From Eq. (11) it results that the θ derivatives of the wave function at $\theta=0$ and π are zero except for $M_N = \pm 1$, which may be at the origin of numerical instabilities. We have to point out, however, that the cosine transform, such as that used in Ref. [21], not only has been tested successfully on model problems (in Ref. [21], for the particular case of $M_N=0$), but also served as the basic technique for the accurate calculation of angular-resolved dissociation probabilities of H_2^+ , with an initial state represented by a linear combination of spherical harmonics with $M_N=0, \pm 1$ [22]. However, it turns out that the inaccuracies

increase when the calculation of angular-resolved kinetic-energy spectra in the ATD regime is attempted. The so-called contact transformation, defined by

$$\Psi_{M_N}(R, \theta, \varphi; t) = \frac{1}{\sqrt{\sin\theta}} e^{iM_N\varphi} \Phi_{M_N}(R, \theta; t), \quad (12)$$

is a way out of the difficulty [bold characters denote the column matrices of Eq. (1)]. Actually, the θ derivative of Φ_{M_N} given by

$$\frac{d}{d\theta} \Phi_{M_N} = \left(\frac{1}{2} \frac{\cos\theta}{\sqrt{\sin\theta}} \Psi_{M_N} + \sqrt{\sin\theta} \frac{d}{d\theta} \Psi_{M_N} \right) e^{-iM_N\varphi} \quad (13)$$

has to be evaluated at $\theta=0$ and π with an angular behavior of Ψ_{M_N} taken as a linear combination of spherical harmonics. The two limiting cases of the θ derivative at $\theta=0$ and π for the spherical harmonics are given by

$$\lim_{\theta \rightarrow 0} Y_{N, \pm M_N}(\theta, \varphi) \simeq (\mp 1)^{M_N} \frac{e^{iM_N\varphi}}{2^{M_N} M_N!} \left[\frac{(2N+1)}{4\pi} \frac{(N+M_N)!}{(N-M_N)!} \right]^{1/2} \theta^{M_N}, \quad (14)$$

$$\lim_{\theta \rightarrow \pi} Y_{N, \pm M_N}(\theta, \varphi) \simeq (-1)^N (\pm 1)^{M_N} \frac{e^{iM_N\varphi}}{2^{M_N} M_N!} \left[\frac{(2N+1)}{4\pi} \frac{(N+M_N)!}{(N-M_N)!} \right]^{1/2} \times (\pi - \theta)^{M_N}. \quad (15)$$

The resulting derivatives for Φ_{M_N} behave like

$$\lim_{\theta \rightarrow 0} \frac{d}{d\theta} \Phi_{\pm M_N}(\theta, \varphi) \simeq (\mp 1)^{M_N} \frac{1}{2^{M_N} M_N!} \left[\frac{(2N+1)}{4\pi} \frac{(N+M_N)!}{(N-M_N)!} \right]^{1/2} \times \left(M_N + \frac{1}{2} \right) \theta^{(M_N-1/2)}, \quad (16)$$

$$\lim_{\theta \rightarrow \pi} \frac{d}{d\theta} \Phi_{\pm M_N}(\theta, \varphi) \simeq (-1)^N (\pm 1)^{M_N} \frac{1}{2^{M_N} M_N!} \left[\frac{(2N+1)}{4\pi} \frac{(N+M_N)!}{(N-M_N)!} \right]^{1/2} \times (M_N - 1) (\pi - \theta)^{(M_N-1/2)}, \quad (17)$$

leading to a cancellation at both ends of the interval $[0, \pi]$ for all positive values of M_N (except $M_N=0$). Thus numerical instabilities related to the cosine Fourier transform performed on the wave function Ψ_{M_N} (with $M_N = \pm 1$) can easily be removed by applying the procedure to Φ_{M_N} , obtained from Ψ_{M_N} , through the contact transformation. It remains,

however, that for $M_N=0$, where the contact transformation fails in producing zero derivatives and the ends of the θ interval, the original procedure of Ref. [21] provides accurate results. The conclusion that can be drawn is that the contact transformation may advantageously be combined with the cosine Fourier transform for all M_N , except $M_N=0$, for which the cosine transform has to be used alone.

When Ψ_{M_N} given by Eq. (12) is introduced into the Schrödinger equation (1) one gets

$$i\hbar \frac{d}{dt} \Phi_{M_N}(R, \theta; t) = [\mathbf{1}(T_R + \tilde{T}_\theta) + \tilde{\mathbf{W}}_{M_N}(R, \theta; t)] \Phi_{M_N}(R, \theta; t), \quad (18)$$

where the rotational kinetic operator is merely

$$\tilde{T}_\theta = -\frac{\hbar^2}{2mR^2} \frac{d^2}{d\theta^2} \quad (19)$$

and the effective potential

$$\tilde{\mathbf{W}}_{M_N}(R, \theta; t) = \mathbf{W}(R, \theta; t) - \frac{\hbar^2}{2mR^2} \mathbf{1} + \frac{\hbar^2}{2mR^2} \frac{M_N^2 - 1/4}{\sin^2\theta} \mathbf{1}. \quad (20)$$

The propagator technique itself has been described within great detail in previous works [21,22] and is based on the repeated use of the short time propagator $\tilde{U}(\delta t)$:

$$\begin{aligned} \Phi_{M_N}(R, \theta; t + \delta t) &= \tilde{U}(\delta t) \Phi_{M_N}(R, \theta; t) \\ &= \exp \left[-\frac{i}{\hbar} [\mathbf{1}(T_R + \tilde{T}_\theta) + \tilde{\mathbf{W}}_{M_N}(t)] \delta t \right] \\ &\quad \times \Phi_{M_N}(R, \theta; t). \end{aligned} \quad (21)$$

Since the three operators T_R , \tilde{T}_θ , and $\tilde{\mathbf{W}}_{M_N}$ do not commute, the exponential on the right-hand side of Eq. (21) is split into five terms using the Moyal formula [29] in a third-order approximation $O(\delta t^3)$. More sophisticated splittings, such as that described by Bandrauk and Shen [30] and leading to higher-order approximations, may be used at this level with the advantage of a larger time step. The propagation of the wave function results from the evaluation of five exponential operators in a way that maintains unitarity and does not involve matrix multiplications. The simple form of \tilde{T}_θ allows a treatment similar to that of T_R . In practical computations, the procedure starts with the action of the potential operator $\tilde{\mathbf{W}}_{M_N}$ on the coordinate representation wave function; the result is cosine transformed in θ such that the angular kinetic operator \tilde{T}_θ is applied. The resulting wave function is Fourier transformed in R , i.e., in a momentum representation suitable for a local action of T_R . The cycle is completed by an inverse Fourier transform in R , action of \tilde{T}_θ , inverse cosine transform in θ , and action of $\tilde{\mathbf{W}}_{M_N}$.

B. Asymptotic analysis

Until very recently the calculation of kinetic-energy spectra involved the propagation of the full wave packet on very large grids, during the total pulse duration, such that the postpulse analysis leads to free fragment properties. The asymptotic analysis consists either in Fourier transforms of the wave-packets [31], in projecting the wavepackets on the continuum eigenfunctions of the field-free Hamiltonian [32], or even in energy-resolved fluxes [33]. The overall procedures are very time consuming because of large grid extensions required to describe the wavepackets during the field interaction, especially when considering asymptotically diverging couplings. The basic idea to describe the wavepacket motion on a restricted grid is the splitting of the wave function into an internal and an asymptotic part, the propagation in the latter being done analytically even during the field interaction [19,22]. The model has been worked out in a one-dimensional case [19]; its three-dimensional generalization constitutes the purpose of this section, and will be followed by an application to H_2^+ photodissociation.

A general and comprehensive overview of the method can be provided by considering two distances: namely, R_{\max} , which fixes, definitively, the total extension of the grid, and R_S which delineates the boundary between the inner and the asymptotic regions. More precisely, the asymptotic region boundary R_S is defined by almost constant or negligible potential energies [$V_{g \text{ or } u}(R \geq R_S) = 0$] as compared to the kinetic energy of the fragments. R_{\max} has to be taken larger than R_S . The initial wave function $\Psi_j(R, \theta; t=0)$ (the index M_N is dropped for simplicity and $j=1,2$ designates g and u , respectively) is sampled on the R, θ grids ($R \in [0, R_{\max}]$ and $\theta \in [0, \pi]$) and propagated using the method described in Sec. II A for solving numerically the coupled wave-packet motion [Eq. (1)]. This procedure is stopped at a time t_i , when the probability amplitude at R_{\max} reaches a given small value ϵ_a :

$$|\Psi_j(R_{\max}, \theta; t_i)| \geq \epsilon_a. \quad (22)$$

Starting at that time, the asymptotic analysis proceeds by splitting wave functions into two parts:

$$\Psi_j(R, \theta; t_i) = \Psi_j^I(R, \theta; t_i) + \Psi_j^A(R, \theta; t_i) \quad (j=1,2) \quad (23)$$

(I for inner and A for asymptotic). Practically, this is done by using a smooth window function $g(R)$ of spatial extension σ , equal to 1 or 0 in the inner or asymptotic regions, respectively [34]:

$$g(R) = \begin{cases} 1 & \text{for } R < R_S \\ 1 - \sin^2\left(\frac{\pi(R - R_S)}{2\sigma}\right) & \text{for } R_S \leq R \leq R_S + \sigma \\ 0 & \text{for } R > R_S + \sigma \end{cases} \quad (24)$$

and

$$\Psi_j^I(R, \theta; t_i) = g(R) \Psi_j(R, \theta; t_i), \quad (25a)$$

$$\Psi_j^A(R, \theta; t_i) = [1 - g(R)] \Psi_j(R, \theta; t_i). \quad (25b)$$

The further evolution is performed, on the one hand, by starting again the previous numerical procedure with the inner part of the wave packet (25a) as an initial wave function and, on the other hand, by the analysis of the asymptotic part of the wave packet (25b) in a way that will be discussed now. The full time propagation consists in the iteration of this basic scheme until convergence is achieved when coherently resumming asymptotic components.

The linearity of the Schrödinger equation allows the separate propagations of Ψ_j^I and Ψ_j^A , the latter being described by

$$i\hbar \frac{d}{dt} \begin{pmatrix} \Psi_1^A \\ \Psi_2^A \end{pmatrix} = \begin{pmatrix} T_R & -\frac{1}{2}e\mathcal{E}(t)R \cos\theta \\ -\frac{1}{2}e\mathcal{E}(t)R \cos\theta & T_R \end{pmatrix} \times \begin{pmatrix} \Psi_1^A \\ \Psi_2^A \end{pmatrix}. \quad (26)$$

This equation results from the asymptotic form of Eq. (1) where, for $R \geq R_S$, T_θ and \tilde{W}_{M_N} are neglected due to the R^{-2} factor and negligible potential terms $V(R)$ as compared to the kinetic energy T_R , particularly important in multiphoton processes leading to high-energy fragments. The amplitude of the neglected R^{-2} terms basically depends upon the rotational excitation of the molecule, which may increase with the laser intensity. This is why R_S is in principle intensity dependent. We incidentally note that although for $\theta=0$ or π the potential operator may diverge when using a contact transformation [cf. Eq. (20)], it is rather its action on the accordingly decreasing wave function that has to be considered, the overall result being zero. The transition dipole moment between the two charge-resonant states is merely given by $\mu(R > R_S) \rightarrow \frac{1}{2}eR$, e being the electron charge. The coupled system (26) can be decoupled by introducing a set of wave functions χ , which are linear combinations of the Ψ_j^A 's:

$$\chi_{1(2)}(R, \theta; t) = \frac{1}{\sqrt{2}} [\Psi_1^A(R, \theta; t) \pm \Psi_2^A(R, \theta; t)] \quad (27)$$

and solutions of

$$i\hbar \frac{d}{dt} \chi_{1(2)}(R, \theta; t) = [T_R \mp \frac{1}{2}e\mathcal{E}(t)R \cos\theta] \chi_{1(2)}(R, \theta; t). \quad (28)$$

We point out the formal analogy between these equations and the ones describing the motion of a free electron in an electric field. R being formally interpreted as the electron

coordinate, Volkov-type solutions [35,36] can be obtained with the functional change

$$\chi_{1(2)}(R, \theta; t) = \exp\left[\pm \frac{i}{\hbar} R \cos\theta \Delta(t, -\infty)\right] \zeta_{1(2)}(R, \theta; t), \quad (29)$$

where

$$\Delta(\tau_2, \tau_1) = \frac{e}{2\hbar} \int_{\tau_1}^{\tau_2} \mathcal{E}(t') dt'. \quad (30)$$

Introducing Eq. (29) into Eq. (28) leads, after straightforward algebra, to the time-dependent evolution equation for ζ ,

$$i\hbar \frac{d}{dt} \zeta_{1(2)}(R, \theta; t) = -\frac{\hbar^2}{2m} \left[\frac{d^2}{dR^2} \pm 2i \cos\theta \Delta(t, -\infty) \frac{d}{dR} - \cos^2\theta \Delta^2(t, -\infty) \right] \zeta_{1(2)}(R, \theta; t), \quad (31)$$

which is solved, in a standard way, by Fourier transforming the two sides of the equality

$$\hat{\zeta}_{1(2)}(k, \theta; t) = \exp\left\{ -\frac{i\hbar}{2m} \int_{t_i}^t [k \pm \cos\theta \Delta(t', -\infty)]^2 dt' \right\} \times \hat{\zeta}_{1(2)}(k, \theta; t_i), \quad (32)$$

with

$$\hat{\zeta}_{1(2)}(k, \theta; t) = \frac{1}{2\pi} \int dR \zeta_{1(2)}(R, \theta; t) e^{-ikR}. \quad (33)$$

Equation (32) is the basic result of the model; it opens the possibility to reach $\Psi_{1(2)}^A$ through Eqs. (27) and (29), by referring to appropriate Fourier transforms. It can easily be shown by Eq. (29) that the Fourier transform of $\chi_{1(2)}$ is related to that of $\zeta_{1(2)}$ by a simple shift of the momentum

$$\hat{\chi}_{1(2)}(k, \theta; t) = \hat{\zeta}_{1(2)}[k \mp \cos\theta \Delta(t, -\infty), \theta; t], \quad (34)$$

so that [Eq. (32) is used]

$$\hat{\chi}_{1(2)}(k, \theta; t) = \exp\left\{ -\frac{i\hbar}{2m} \int_{t_i}^t [k \mp \cos\theta \Delta(t, t')]^2 dt' \right\} \times \hat{\zeta}_{1(2)}[k \mp \cos\theta \Delta(t, -\infty), \theta; t_i]. \quad (35)$$

By recasting $\hat{\zeta}$ in terms of $\hat{\chi}$ Eq. (34), one finally gets the evolution equation for $\hat{\chi}$,

$$\hat{\chi}_{1(2)}(k, \theta; t) = \exp\left\{ -\frac{i\hbar}{2m} \int_{t_i}^t [k \mp \cos\theta \Delta(t, t')]^2 dt' \right\} \times \hat{\chi}_{1(2)}[k \mp \cos\theta \Delta(t, t_i), \theta; t_i]. \quad (36)$$

It is to be noted that in addition to a phase factor, $\hat{\chi}(k, \theta; t)$, at time t , is obtained from $\hat{\chi}(k, \theta; t_i)$ by merely shifting the momentum by the laser pulse area $\Delta(t, t_i)$ weighted by $\cos\theta$.

This factor is precisely the difference between equation Eq. (36) and the corresponding equation (13) of Ref. [19] of the one-dimensional case. The asymptotic wave functions in the momentum space result from Eq. (27):

$$\begin{aligned} \hat{\Psi}_g^A(k, \theta; t) &= \exp\left\{ -\frac{i\hbar}{2m} \int_{t_i}^t [k - \cos\theta \Delta(t, t')]^2 dt' \right\} \\ &\times \{\hat{\chi}_1[k - \cos\theta \Delta(t, t_i), \theta; t_i]\} \\ &+ \exp\left\{ -\frac{i\hbar}{2m} \int_{t_i}^t [k + \cos\theta \Delta(t, t')]^2 dt' \right\} \\ &\times \{\hat{\chi}_2[k + \cos\theta \Delta(t, t_i), \theta; t_i]\}, \end{aligned} \quad (37a)$$

$$\begin{aligned} \hat{\Psi}_u^A(k, \theta; t) &= \exp\left\{ -\frac{i\hbar}{2m} \int_{t_i}^t [k - \cos\theta \Delta(t, t')]^2 dt' \right\} \\ &\times \{\hat{\chi}_1[k - \cos\theta \Delta(t, t_i), \theta; t_i]\} \\ &- \exp\left\{ -\frac{i\hbar}{2m} \int_{t_i}^t [k + \cos\theta \Delta(t, t')]^2 dt' \right\} \\ &\times \{\hat{\chi}_2[k + \cos\theta \Delta(t, t_i), \theta; t_i]\}. \end{aligned} \quad (37b)$$

Equations (37) are the analytical evolution of $\hat{\Psi}_g^A(k, \theta; t)$ from t_i to t . The angular-resolved fragments probability distribution (kinetic-energy spectrum) is given by

$$\mathcal{P}(k, \theta) dk = \lim_{t \rightarrow \infty} [|\hat{\Psi}_g^A(k, \theta; t)|^2 + |\hat{\Psi}_u^A(k, \theta; t)|^2] dk, \quad (38)$$

where $t \rightarrow \infty$ means not only that the laser pulse is switched off but also that there are no outgoing continuum components of the inner-part wave packet.

III. RESULTS

In this section we test the accuracy of the previously presented procedure by applying it to simple model calculations before proceeding to an evaluation of the angular-resolved spectra of H_2^+ irradiated by a linearly polarized laser. We have to point out that the asymptotic matching to Volkov states depends crucially on the accuracy of the phases of the numerically propagated inner region wave packet. This can be controlled by the value of ϵ_a [as defined by Eq. (22)] that starts the splitting and matching procedures. Converged results within less than 1% accuracy are obtained for $\epsilon_a = 10^{-8}$.

A. Numerical tests

We take as an initial wave function $\Psi(t=0)$, the ground vibrational state of H_2^+ written as the product of a radial and an angular part, i.e.,

$$\Psi_{M_N}(t=0) = \chi_{gv=0N=1}(R) Y_{N, M_N}(\theta, \varphi). \quad (39)$$

This wave function is propagated under the effect of the (field-free) ground-state Hamiltonian over 40 fs, our purpose being to check the accuracy of the propagator with respect to

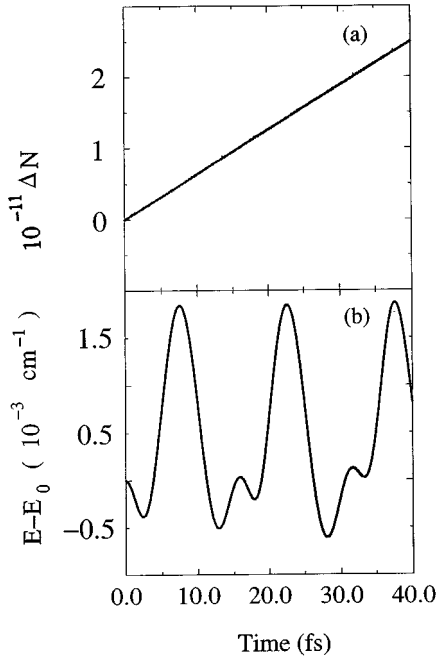


FIG. 1. Norm and energy conservations using Dateo and Metiu's cosine transform [21] for $M_N=0$. Panel (a) is the deviation of the norm from 1 and panel (b) the deviation of the energy (in cm^{-1}) from $E_0 = -21\,234.742\text{ cm}^{-1}$ as a function of propagation time in femtoseconds.

norm and energy conservations. Figure 1 displays the results of the calculation for $M_N=0$, using Dateo and Metiu's cosine transform method. For 64 θ -grid points, one obtains a deviation of the norm $\Delta N(t) = \|\Psi(t)\|^2 - \|\Psi(0)\|^2$, which remains of the order of magnitude of 10^{-11} . Excellent accuracy is reached for the energy conservation. The deviation of the ground-state energy

$$E = \frac{\langle \Psi(t) | H | \Psi(t) \rangle}{\langle \Psi(t) | \Psi(t) \rangle} \quad (40)$$

from its initial value $E_0 = -21\,234.742\text{ cm}^{-1}$, follows a quasiperiodic behavior [Fig. 1(b)] with an oscillation amplitude not exceeding $2 \times 10^{-3}\text{ cm}^{-1}$. The results for $M_N=1$ are gathered in Fig. 2, where the two propagation methods (pure cosine Fourier transform or contact transform combined with the cosine transform) are compared for different number of grid points N_θ . The conclusions are twofold.

(i) Norm and energy conservations are substantially deteriorated during the early dynamics when the cosine transform is used with $N_\theta = 64$ grid points (deviations of the order of 10^{-4} for the norm and not less than 15 cm^{-1} for the energy). The calculations can however be improved by doubling the number of grid points ($N_\theta = 128$). This is especially true for the energy; a better convergence of the cosine Fourier expansion leads to energy deviations within one wave number. The improvement for the norm conservation is less significant.

(ii) Very high accuracies are reached when using the contact transform even for a θ grid not exceeding $N_\theta = 32$ points. The deviation of the norm from its unit value is less than 0.5×10^{-5} and that of the energy less than 0.1 cm^{-1} . These values can even further be improved by doubling the

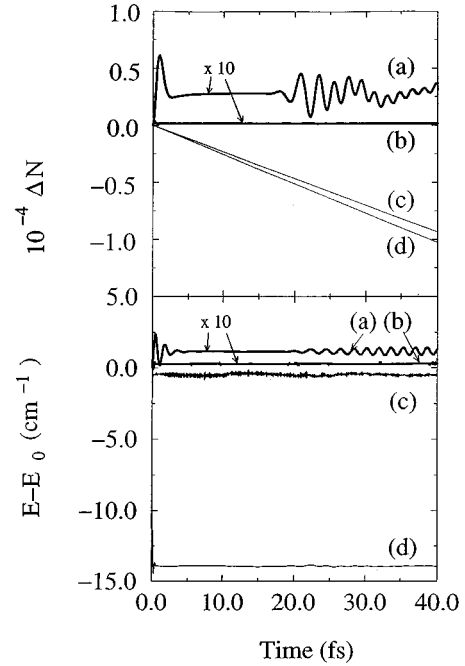


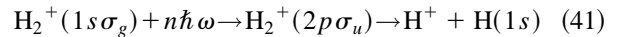
FIG. 2. Norm (upper panel) and energy (lower panel) conservations using Dateo and Metiu's cosine transform [with 64 (curve d) or 128 (curve c) grid points on θ] or the contact transform [with 32 (curve a) or 64 (curve b) grid points on θ] for $M_N=1$. Energies are indicated in cm^{-1} and time in femtoseconds. Note that a scaling factor ($\times 10$) has been introduced for the contact transform.

number of grid points. In particular, calculations with the contact transform and using $N_\theta = 64$ grid points (same as for Fig. 1) lead to accuracies comparable to those of $M_N=0$, obtained with the cosine transform.

B. Angular-resolved spectra (H_2^+ , $\lambda = 532\text{ nm}$)

We are now in a situation to examine the multiphoton alignment dynamics of H_2^+ , irradiated by short and intense laser pulses. This study is basically motivated by a detailed intense field ATD experiment on H_2^+ at $\lambda = 532\text{ nm}$ [5]. The ultimate goal is a thorough understanding of angular-resolved dissociation spectra that reveals some unexpected proton distributions, namely, at some energies, increasing the laser intensity produces less aligned photofragments.

The ground and first excited states that, within the Born-Oppenheimer approximation, describe the photodissociation process



correspond to $(1s\sigma_g)^2\Sigma_g^+$ and $(2p\sigma_u)^2\Sigma_u^+$ symmetries, respectively. The potential-energy curves are taken from Bunkin and Tugov's fit [23] and the electronic transition moment is taken from Bates [24]. The field-dressed potential-energy curves involved in the two main Floquet blocks (shifted by the photon energy corresponding to $\lambda = 532\text{ nm}$) are displayed in their diabatic and adiabatic representations in Fig. 3. The adiabatic representation leading to avoided curve crossing situations results from the diagonalization of the radiative interaction for one of the experimental intensities, i.e., 10^{13} W/cm^2 . By defining the boundary of

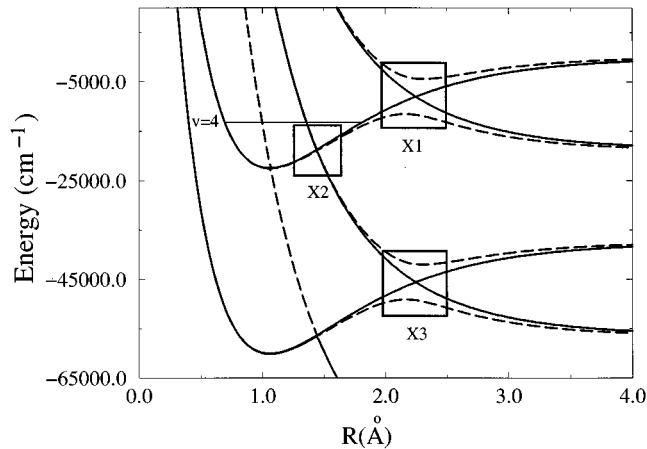


FIG. 3. H_2^+ field-dressed potential-energy curves for $\lambda=532$ nm and $I=10^{13}$ W/cm 2 , in the diabatic (solid line) and adiabatic (broken line) representations. The position of the initial vibrational level $v=4$ is indicated by a thin horizontal line. The rectangle boxes X1,X2,X3 point out the avoided curve crossing regions.

the asymptotic region as $R_S \approx 10$ Å [37] the potential-energy difference $V_g(R) - V_u(R)$, which is exponentially decreasing for $R > R_S$, does not exceed 150 cm $^{-1}$ and remains an order of magnitude less than the fragments kinetic energies resulting from the absorption of 532-nm wavelength photons. This criterion validates the use of Eq. (26) and the channel decoupling associated with Eqs. (27) and (28). We also note that throughout this region the linear R dependence of the transition dipole moment, which is also required for the use of Volkov states, follows within an accuracy better than $10^{-3}\%$ the more complete dipole length formula given by Mulliken in a linear combination of atomic orbitals approximation [15,24].

The laser pulse is taken as a Gaussian [cf. Eq. (7)] with rise and falloff times $\tau=30$ fs, a maximum intensity of 10^{13} W/cm 2 being reached at $t_0=75$ fs. We note, from the consultation of Table 1 of Ref. [38], that for a wavelength of $\lambda=532$ nm and an intensity of 5×10^{14} W/cm 2 the ionization rate is 1.3×10^{12} s $^{-1}$, which means that we can safely neglect it (as long as for an intensity of 10^{13} W/cm 2 we are discussing excitation and dissociation processes occurring on a femtosecond time scale).

An overall dynamical view is displayed in Figs. 4 and 5 in terms of three-dimensional graphs representing, at different detection times ranging from $t=100$ fs (just after the pulse maximum) up to $t=290$ fs (time for converged spectrum calculations), relative dissociation probabilities as a function of the fragments kinetic energies and angular distributions. The scaling factors indicate the relative contributions of the spectrum at a given time to the final one. As an example, the spectrum recorded at time $t=230$ fs roughly contributes one-tenth to the final result. The calculations are presented for two cases where $N=1$, $M_N=0$ (Fig. 4, using the method of Ref. [21]) and $N=1$, $M_N=1$ (Fig. 5, using contact transform) and for an initial vibrational state $v=4$, located near the top of the field-lowered potential barrier leading to the one-photon dissociation channel (as depicted in Fig. 3). Some general observations are in order.

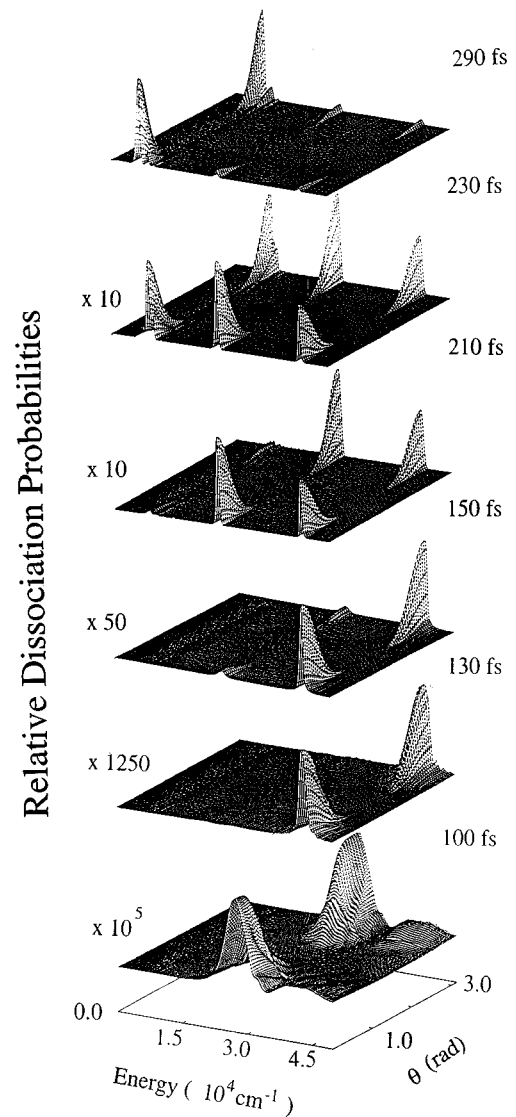


FIG. 4. Relative dissociation probabilities for $M_N=0$ as a function of protons kinetic energies (in cm $^{-1}$) and detection angles (in radians), for different detection times (in femtoseconds, on the right-hand side of each 3D graph). Note that the scaling factors on the left are with respect to the bottom graph ($t=290$ fs).

(i) At $t=100$ fs, dissociation rates are still negligible, with angular distributions roughly reflecting those of the spherical harmonics $Y_{1,0} \propto \cos \theta$ (for $M_N=0$, Fig. 4) or $Y_{1,1} \propto \sin \theta$ (for $M_N=1$, Fig. 5).

(ii) At $t=130$ fs, high-velocity photofragments are the first to be collected at energies corresponding to the absorption of three photons.

(iii) Between $t=150$ and 210 fs, less energetic (slower) fragments corresponding to the net absorption of two photons are detected, in amounts that even exceed the ones collected in the so-called three-photon peak. Moreover, a stabilization is observed for the two- and three-photon peak populations, their relative branching ratios already being time independent.

(iv) Low-velocity fragments reach detection distances at even later times ($t=230$ fs) and contribute to the one-photon peak.

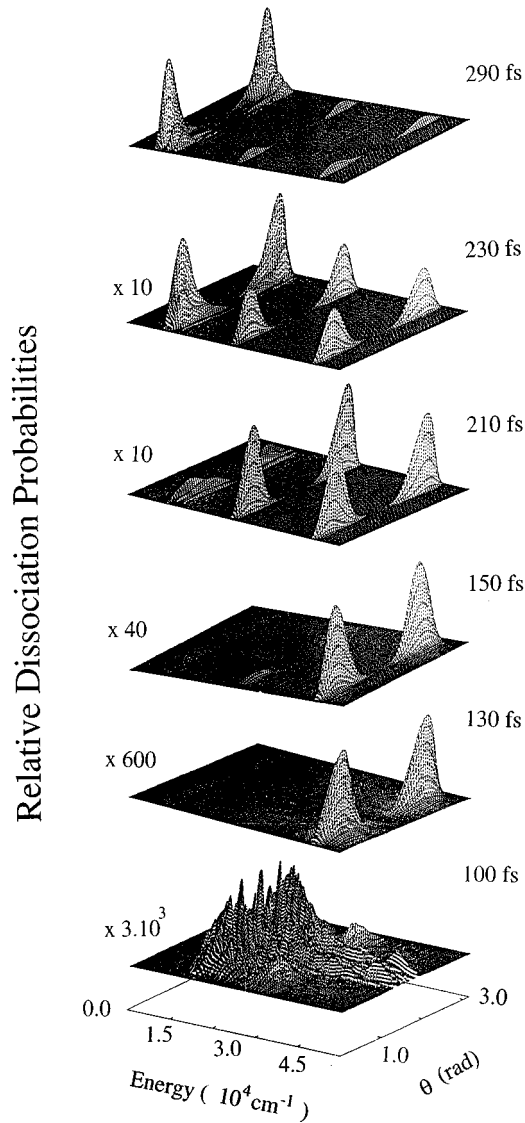


FIG. 5. Same as for Fig. 4, but for $M_N=0$.

(v) Final stabilized spectra at $t=290$ fs reflect the leading one-photon process with a peak height roughly ten times the one corresponding to the two- or three-photon maxima. Small satellite peaks at roughly 2000 cm^{-1} from the one-photon maximum are also recorded. These energy differences reflect the vibrational level separations of H_2^+ . The satellite structures may thus correspond to the nonadiabatic excitation of resonances correlating with the $v=5$ or 6 levels of a field-free situation [39]. However, they are absent in one-dimensional (fixed angle) spectrum calculations, supporting the argument that they are rather to be associated with some Coriolis effect, coupling the rotational and vibrational motions.

(vi) The total dissociation rate is five times larger for $M_N=0$ (0.29×10^{-3}) than for $M_N=1$ (0.59×10^{-4}). This is consistent with the fact that the leading one-photon mechanism proceeds through a barrier tunneling that favors the dissociation of the initial $Y_{10}(\theta, \varphi)$ distribution peaked at $\theta=0$ and π by the radiative interaction lowering efficiently the barrier precisely at these angles.

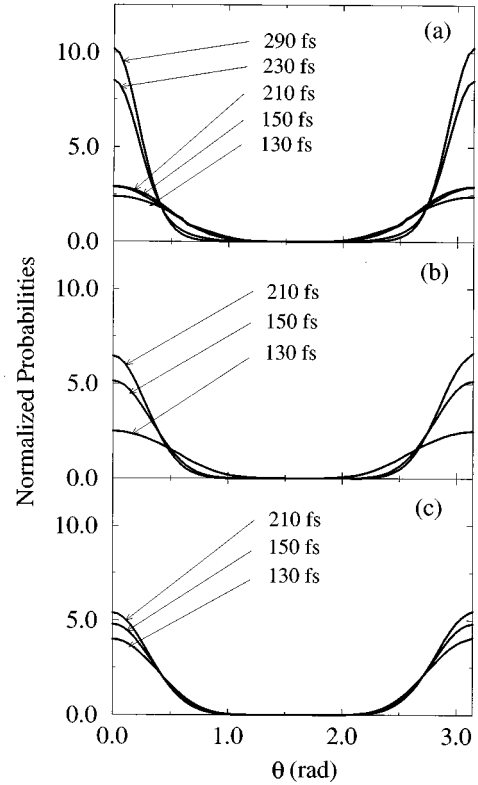


FIG. 6. Normalized angular distributions, for $M_N=0$ and for the different detection times of Figs. 4 and 5. Results are displayed for (a) the one-photon peak, (b) the two-photon peak, and (c) the three-photon peak.

The temporal evolution of the alignment patterns is further detailed in Fig. 6 for $M_N=0$ and in Fig. 7 for $M_N=1$ in terms of θ -dependent normalized probabilities defined by

$$\mathcal{P}_i(\theta; t) = \frac{\int_{E_i - \epsilon_i}^{E_i + \epsilon_i} dE |\Psi_E(\theta; t)|^2}{\int_0^\pi d\theta \sin\theta \int_{E_i - \epsilon_i}^{E_i + \epsilon_i} dE |\Psi_E(\theta; t)|^2}, \quad (42)$$

i being an index for the one-, two-, and three-photon peaks, with a maximum at E_i and an energy range of $2\epsilon_i$.

Two major points can be outlined.

(i) The laser-induced alignment increases with time (as compared to the weak-field reference distribution of $\frac{3}{2}\cos^2\theta$), following the intuitive expectation that lately detected slow fragments interacting over a longer period with the laser are better aligned. This alignment is rather progressive in time for the three- and two-photon peaks and stabilized at $t=210$ fs [panels (a) and (b) of Figs. 6 and 7]. A somewhat different dynamics affects the fragments contributing to the one-photon peak: their angular distributions [panel (a)] are very much modified after $t=210$ fs showing a rapid transition from nearly “stabilized” isotropic distributions (between $t=150$ and 210 fs) to sharply aligned ones at later times. This again is in relation to the barrier lowering. Only negligible amounts of fragments are detected in the one-photon channel at early times, presumably resulting from more complicated multiphoton exchanges. The major and

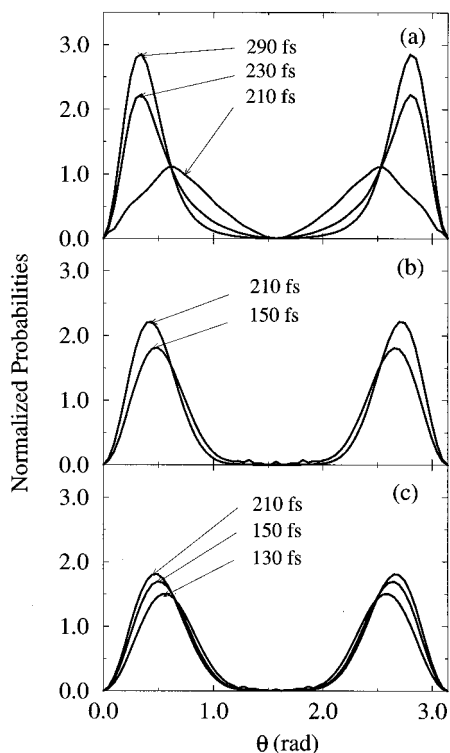


FIG. 7. Same as for Fig. 6, but for $M_N=1$.

late ($t > 210$ fs) contribution to the one-photon peak in the spectrum comes from low-velocity fragments that have been aligned by the field through the dynamical bond softening mechanism very efficiently for $\theta=0, \pi$ and for the pulse peak intensity [22].

(ii) From the comparison of the angular distributions of each photon peak, a general tendency seems to emerge, namely, the fragments contributing to the one-photon peak are noticeably more aligned than the others and, to a certain extent, the ones of the two-photon peak are more aligned than the three-photon peak.

An interpretation can be provided by comparing the alignment dynamics of the two laser-induced mechanisms responsible for the dissociation, which are in competition: the barrier lowering and the nonadiabatic transition. The avoided

curve crossing regions where these mechanisms take place are indicated by the boxes of Fig. 3. X1 delineates the adiabatic potential barrier lowering region. The radiative interaction $\mu \sqrt{I} \cos \theta$ is stronger for $\theta=0$ and π and the dissociation is enhanced in these directions. In a dynamical viewpoint, the torque that is exerted by the laser on the molecule allows the wave packet to skirt around the potential barrier and find the minimum-energy pathway towards the dissociative valley (that is, for directions close to $\theta=0$ or π). Fragments resulting from this one-photon process have low velocity and contribute to the one-photon peak in the spectrum; they are highly aligned with the laser polarization axis. Insofar as the pulse intensity is not strong enough for the barrier to be lowered (during its rise time, for instance) the dissociation can only proceed through nonadiabatic transitions depicted by the X2 and X3 boxes. As has been discussed previously [22], such transitions between adiabatic states (obtained by the diagonalization of radiative interactions) are monitored by the so-called nonadiabatic couplings reaching their maximum amplitude for $\theta \approx \pi/2$ (corresponding to the minimum of the radiative interaction or diabatic couplings). The validity of an adiabatic representation for X2 is probably not so clear due to a rather weak third-order matter-field coupling. Molecules already aligned with the laser are however expected to undergo a more efficient Franck-Condon diabatic transition and proceed through the two-photon adiabatic channel. However the resulting alignment of the two-photon peak is not enhanced, as in the case of the one-photon peak, by the dynamical effect due to the barrier lowering at X1: the fragments contributing to the two-photon peak are less aligned than those of the one-photon peak. For X3, involving a strong first-order coupling, the adiabatic frame is appropriate. A nonadiabatic transition (maximum for $\theta \approx \pi/2$) allows one to reach the three-photon channel, the outcome being a more isotropic distribution of high-velocity fragments contributing to the three-photon peak.

ACKNOWLEDGMENT

We acknowledge a grant of computing time on CRAY C-98 from the Institut du Developpement et des Ressources en Informatique Scientifique under Project No. 970425.

-
- [1] R. M. Potvliege and R. Shakeshaft, in *Non Perturbative Treatment of Multiphoton Ionization within the Floquet Framework*, edited by M. Gavrilu (Academic, New York, 1992).
- [2] *Coherence Phenomena in Atoms and Molecules in Laser Fields*, Vol. 287 of *NATO Advanced Study Institute, Series B: Physics*, edited by A. D. Bandrauk and S. C. Wallace (Plenum, New York, 1992).
- [3] P. H. Bucksbaum, A. Zavriyev, H. G. Muller, and D. W. Schumacher, *Phys. Rev. Lett.* **54**, 1883 (1990).
- [4] A. Giusti-Suzor, X. He, O. Atabek, and F. H. Mies, *Phys. Rev. Lett.* **64**, 515 (1990).
- [5] A. Zavriyev, P. H. Bucksbaum, H. G. Muller, and D. W. Schumacher, *Phys. Rev. A* **42**, 5500 (1990).
- [6] B. Yang, M. Saeed, L. F. Di Mauro, A. Zavriyev, and P. H. Bucksbaum, *Phys. Rev. A* **44**, R1458 (1991).
- [7] D. Normand, L. A. Lompré, and C. Cornaggia, *J. Phys. B* **25**, L497 (1992).
- [8] K. Codling and L. J. Frasinski, *J. Phys. B* **26**, 783 (1993).
- [9] S. J. Chu, *J. Chem. Phys.* **75**, 2215 (1981).
- [10] H. D. Feit, J. A. Fleck, and A. Steiger, *J. Comput. Phys.* **47**, 412 (1982).
- [11] H. D. Feit and J. A. Fleck, Jr., *J. Chem. Phys.* **78**, 301 (1983); **80**, 2578 (1984).
- [12] R. W. Heather and F. H. Mies, *Phys. Rev. A* **44**, 7560 (1991).
- [13] G. Jolicard and O. Atabek, *Phys. Rev. A* **46**, 5845 (1992).
- [14] T. T. Nguyen Dang, F. Chateaneuf, O. Atabek, and X. He, *Phys. Rev. A* **51**, 1387 (1993).
- [15] R. S. Mulliken, *J. Chem. Phys.* **7**, 20 (1939).

- [16] D. E. Ramaker and J. M. Peck, *At. Data* **5**, 167 (1973).
- [17] M. Y. Ivanov and P. B. Corkum, *Phys. Rev. A* **48**, 580 (1993).
- [18] R. Lefebvre and O. Atabek, *Int. J. Quantum Chem.* **63**, 403 (1997).
- [19] A. Keller, *Phys. Rev. A* **52**, 1450 (1995).
- [20] R. Heather and H. Metiu, *J. Chem. Phys.* **86**, 5009 (1987).
- [21] C. E. Dateo and H. Metiu, *J. Chem. Phys.* **95**, 7392 (1991).
- [22] R. Numico, A. Keller, and O. Atabek, *Phys. Rev. A* **52**, 1298 (1995).
- [23] F. V. Bunkin and I. I. Tugov, *Phys. Rev. A* **8**, 601 (1973).
- [24] D. R. Bates, *J. Chem. Phys.* **19**, 1122 (1951).
- [25] R. Kosloff, *J. Phys. Chem.* **92**, 2087 (1988).
- [26] R. C. Mowrey and D. J. Kouri, *J. Chem. Phys.* **84**, 6466 (1986); **86**, 2087 (1987).
- [27] R. Almeida, C. E. Dateo, V. Engel, and H. Metiu, *Comput. Phys. Commun.* **63**, 435 (1991).
- [28] D. A. Varshalovich, A. N. Moskalev, and V. K. Khersonskii, *Quantum Theory of Angular Momentum* (World Scientific, Singapore, 1988).
- [29] J. E. Moyal, *Proc. Cambridge Philos. Soc.* **45**, 99 (1949).
- [30] A. D. Bandrauk and H. Shen, *J. Chem. Phys.* **99**, 1185 (1993).
- [31] E. E. Aubanel, J. M. Gauthier, and A. D. Bandrauk, *Phys. Rev. A* **48**, 2145 (1993).
- [32] E. Charron, A. Giusti-Suzor, and F. H. Mies, *Phys. Rev. Lett.* **71**, 692 (1993).
- [33] J. Perie and G. Jolicard, *J. Phys. B* **26**, 4491 (1993).
- [34] Note that this shape for a continuous and derivable window function is an improvement over the functional forms previously considered in the sense that it optimizes the undesired wave-packet reflections.
- [35] L. V. Keldysh, *Zh. Éksp. Teor. Fiz.* **47**, 1945 (1964) [*Sov. Phys. JETP* **20**, 1307 (1965)].
- [36] H. R. Reiss, *Phys. Rev. A* **22**, 1786 (1980).
- [37] T. Zuo, S. Chelkowski, and A. D. Bandrauk, *Phys. Rev. A* **49**, 3943 (1994).
- [38] H. Yu and A. D. Bandrauk, *J. Chem. Phys.* **102**, 1257 (1995).
- [39] R. Numico, A. Keller, and O. Atabek, *Phys. Rev. A* **56**, 772 (1997).